

Structure and dynamics of multicellular assemblies measured by coherent light scattering

This content has been downloaded from IOPscience. Please scroll down to see the full text.

2017 New J. Phys. 19 073033

(<http://iopscience.iop.org/1367-2630/19/7/073033>)

View [the table of contents for this issue](#), or go to the [journal homepage](#) for more

Download details:

IP Address: 86.246.136.23

This content was downloaded on 17/08/2017 at 09:34

Please note that [terms and conditions apply](#).

You may also be interested in:

[Digital Fourier microscopy for soft matter dynamics](#)

Fabio Giavazzi and Roberto Cerbino

[Advances in the microrheology of complex fluids](#)

Thomas Andrew Waigh

[Collective cell migration: a physics perspective](#)

Vincent Hakim and Pascal Silberzan

[Advantages of a logarithmic sampling scheme for XPCS experiments at the European XFEL using the AGIPD detector](#)

J Becker and H Graafsma

[Collective cell motion in endothelial monolayers](#)

A Szabó, R Ünneper, E Méhes et al.

[Observation of coherent backscattering of light by coldatoms](#)

G Labeyrie, C A Müller, D S Wiersma et al.

[The application of dynamic light scattering to complex plasmas](#)

Andreas Aschinger and Jörg Winter

[Simulation study of the impact of AGIPD design choices on X-ray Photon Correlation Spectroscopy utilizing the intensity autocorrelation technique](#)

J Becker, C Gutt and H Graafsma

[Fluctuation microscopy: a probe of medium range order](#)

M M J Treacy, J M Gibson, L Fan et al.



PAPER

Structure and dynamics of multicellular assemblies measured by coherent light scattering

OPEN ACCESS

RECEIVED

7 March 2017

REVISED

13 June 2017

ACCEPTED FOR PUBLICATION

22 June 2017

PUBLISHED

27 July 2017

Original content from this work may be used under the terms of the [Creative Commons Attribution 3.0 licence](#).

Any further distribution of this work must maintain attribution to the author(s) and the title of the work, journal citation and DOI.



Benjamin Brunel¹, Carles Blanch², Aurélien Gourrier¹ , Vanni Petrolli¹, Antoine Delon¹, Jean-François Joanny^{2,3}, Rémi Carminati⁴, Romain Pierrat^{4,5} and Giovanni Cappello^{1,5}

¹ Université Grenoble Alpes, Laboratoire Interdisciplinaire de Physique, CNRS, F-38000 Grenoble, France

² Institut Curie, CNRS, Université P. et M. Curie, UMR 168, F-75231 Paris, France

³ ESPCI Paris, PSL Research University, 10 rue Vauquelin, F-75005 Paris, France

⁴ ESPCI Paris, PSL Research University, CNRS, Institut Langevin, 1 rue Jussieu, F-75005 Paris, France

⁵ Authors to whom any correspondence should be addressed. Theory: Romain Pierrat and experiments: Giovanni Cappello.

E-mail: romain.pierrat@espci.fr and giovanni.cappello@univ-grenoble-alpes.fr

Keywords: dynamic light scattering, multicellular structures, coherent optics

Abstract

Determining the structure and the internal dynamics of tissues is essential to understand their functional organization. Microscopy allows for monitoring positions and trajectories of every single cell. Those data are useful to extract statistical observables, such as intercellular distance, tissue symmetry and anisotropy, and cell motility. However, this procedure requires a large and supervised computational effort. In addition, due to the large cross-section of cells, the light scattering limits the use of microscopy to relatively thin samples. As an alternative approach, we propose to take advantage of light scattering and to analyze the dynamical diffraction pattern produced by a living tissue illuminated with coherent light. In this article, we illustrate with a few examples that supra-cellular structures produce an exploitable diffraction signal. From the diffraction signal, we deduce the mean distance between cells, the anisotropy of the supra-cellular organization and, from its fluctuations, the mean speed of moving cells. This easy to implement technique considerably reduces analysis time, allowing real time monitoring.

1. Introduction

In this article, we describe a non-imaging approach to investigate the structure and dynamics of living multicellular structures. The proposed method is based on the analysis of the dynamic speckle pattern produced by a set of cells illuminated with coherent light.

Determining the structure and the internal dynamics of tissues is essential to understand their functional organization. In fact many of their features, such as symmetry and topology, cannot be inferred from those of the composing cells [1]. Conversely, long range self-organization also emerges from cell division, migration and death [2]. Video microscopy allows to monitor such complex cascade of events in great details and the analysis of the acquired time sequence of images provides accurate measures of position, shape and trajectory of each cell inside the tissue, from birth to death [3]. Nevertheless, in most instances, the net result of such analytical procedures is to reduce those large data to only a few statistical observables, such as the mean cell-to-cell distance, the local/global symmetry or anisotropy of the tissue and the crawling speed of the cells or their diffusion coefficient. Here, we propose to directly measure these observables by analyzing the dynamical speckle pattern produced by a living tissue illuminated with a collimated laser beam. The drawback of this self-averaging method is to lose the cell-to-cell heterogeneity, which might be crucial in certain circumstances.

Light, x-ray and neutron scattering are long-time known and widely used tools to investigate microscopic to nanoscopic structures [4–6]. In biology, light scattering has been used to measure single cell size or nucleus size *in vitro* [7, 8] and more recently *in vivo* [9]. Light scattering is not limited to structure identification and many light scattering-based methods have emerged in biology [10]. One of them is speckle analysis or dynamic light

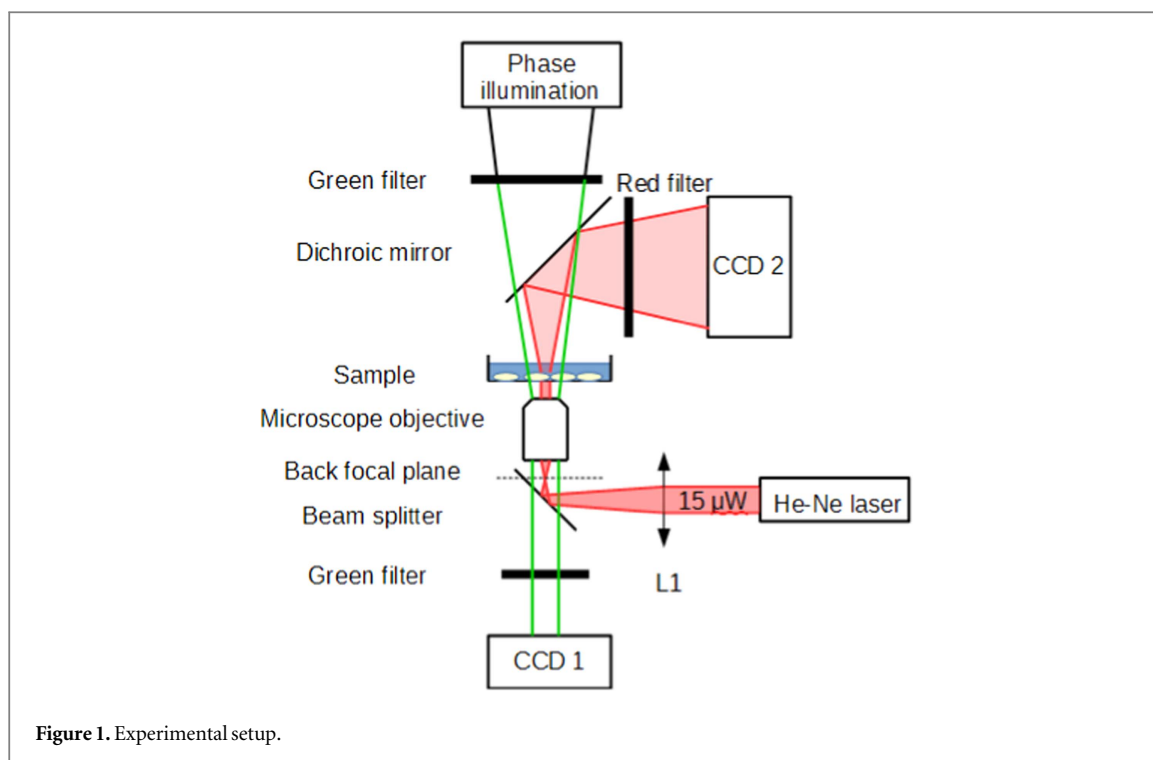


Figure 1. Experimental setup.

scattering (DLS), which was already well-established in soft matter [11–13]. In the multiple scattering regime, it has been used for functional imaging such as the measure of brain activity [14–16]. While DLS has also been applied to characterize internal cells dynamics [17–19] or cellular suspensions [20], its use for the investigation of multicellular structures remains very limited [21]. This is mainly due to the fact that the analysis can be performed by directly visualizing the cells with classical microscopy, while the interpretation of the speckle pattern in reciprocal space is, in principle, a non-trivial task that requires solving an inverse problem through modeling and computational efforts. Nevertheless, we have several reasons to believe that this approach is extremely promising to investigate tissue dynamics:

- (i) The large scattering produced by cells, which severely limits the use of microscopy in case of thick samples, intrinsically carries structural information that can be analyzed by DLS and, thus, becomes an advantage.
- (ii) Because of the intrinsic scattering contrast in cells, this approach does not require preliminary staining. With no constraints imposed by the fluorescent dyes, the illumination wavelength can be tuned to maximize the penetration depth (near infrared) in 3D samples, whose thickness is limited by light scattering. This also makes the technique suitable to investigate primary living tissues.
- (iii) Speckle analysis inherently averages the statistical observable over the whole cell population, which size is determined by the illumination area (1 μm –1 mm).
- (iv) As multicellular structures scatter strongly even with low illumination (<100 nW/cell), DLS allows fast and long acquisitions with reduced photo-damage. On the other hand, one could also increase the illumination power to image samples that strongly absorb light.

In this article, we propose several examples illustrating how to extract the structural and dynamic features of a multicellular ensemble, from time resolved speckle patterns.

2. Methods

2.1. Experimental setup

The setup bears some similarities to earlier one designed by *Suissa et al* [17]. In order to combine phase contrast imaging and speckle analysis, the experimental setup was based on an inverted Zeiss Axiovert 100 microscope (figure 1). The microscope was equipped with a phase-contrast condenser, a 10 \times objective (Zeiss EC Plan-Neofluar, N.A. 0.3) and a charge-coupled device camera (CCD1; Allied Vision Guppy). To generate a speckle pattern, the sample was illuminated using an attenuated (2.0 ND; Thor Labs) He-Ne laser (Uniphase 1101,

1.5 mW, 633 nm) focused on the back focal plane of the objective using an achromatic lens (L1: $f = +100$). In this way, we illuminated the sample with a Gaussian beam, with a divergence of ~ 0.01 rad and a width on the sample of about $80 \mu\text{m}$ (FWHM). The speckle pattern was collected on a second charge-coupled device camera (CCD2; Allied Vision Pike F 046B) positioned as close as possible above the sample (sample to detector distance: 77.7 mm). At this position, the CCD2 camera collected the scattered light for angles up to 7° , corresponding to $q < 1.2 \mu\text{m}^{-1}$, with an angular resolution of 0.007° ($0.001 \mu\text{m}^{-1}$) per pixel. Angles inferior to 0.3° ($q < 0.05 \mu\text{m}^{-1}$) were also inaccessible because of the laser divergence. Angular calibration was performed using a diffraction grating. To combine phase-contrast imaging and speckle analysis, we used two different wavelengths. We added a monochromatic filter (550 nm) above the condenser and separated the two optical paths with a beam splitter and a dichroic mirror (700–900 nm pellicle beam splitter; ThorLabs).

2.2. Cell culture

CT26 (mice colon carcinoma) cells were used and cultured at 37°C and 5% CO_2 in a DMEM (gibco Life technologies) medium supplemented with 10% of fetal bovine serum and 1% Penicillin-Streptomycin (Sigma). Cells were detached from flask using trypsin, resuspended in medium and seeded in a 35 mm VWR round petri dish.

2.3. Adherent stripes

In order to artificially arrange cells in lines, we used adherent micropatterned substrates fabricated as described in [22]. Adherent stripes were prepared on 32 mm round glass coverslips, which surface had previously been cleaned and activated with an air plasma cleaner (exposure: 5 min at 0.2 mbar). To create non-adherent surfaces, the coverslips were coated with a 0.1 mg ml^{-1} pLL-PEG solution in 10 mM HEPES buffer at pH 7.4 (incubation time 30 min). Then, to create the patterns (local degradation of the pLL-PEG coating) the coverslips were exposed to UV light (190 nm) through a photolithography mask (chromium on quartz) with the appropriate pattern geometry for 5 min at 6 mW cm^{-2} . The patterned coverslips were eventually incubated for 30 min in a ECM protein solution ($20 \mu\text{g ml}^{-1}$ fibronectin, $20 \mu\text{g ml}^{-1}$ fluorescently labeled fibrinogen in 100 mM sodium bicarbonate). Proteins only adsorb on the pLL-PEG free regions thus promoting selective cell adhesion. The patterned coverslips were shortly stored in PBS buffer at 4°C .

2.4. DLS and tracking

In order to measure the intensity-intensity autocorrelation function, frames were acquired every 20 s over a period of at least 90 min. For isotropic samples (2D), only the absolute value of the scattering vector is relevant, thus correlation functions were averaged over pixels located in a ring corresponding to a given q value. The characteristic size of speckles on the CCD was about 650 pixels, so that q -rings contained between 230 (inner ring) and 890 (outer ring) speckles. For 1D sample, correlation functions were averaged over 20×20 pixels squares, containing approximately 3 speckles of 120 pixels area. Then for a given q value in a direction, results located in a rectangle centered on the direction axis (60 pixels along the direction, 40 pixels perpendicularly) were averaged. We limited our analysis to $q > 0.1 \mu\text{m}^{-1}$ because the laser beam saturates the CCD. If readers are interested in ultralow angles, we recommend them to refer to [23]. To assess results obtained by DLS, we manually tracked cell motion, by clicking on their nuclei on each frame of the movie to get the trajectory $[x(t), y(t)]$. Then, the instantaneous speed is computed for each cell from its trajectory and averaged over the whole set of trajectories.

2.5. Simulations

In addition to experiments, numerical simulations of the multicellular system were performed. We used a simple run and tumble-like model to capture the motion of individual cells in 2D environments. We ignored the internal structure of cells, modeling them as point-like objects, and avoided physical interactions between them using a dilute approximation. Hence our individual particles were allowed to lie in two states: either motile or quiescent. In the first state, the speed v followed a narrow Gaussian distribution with mean value \bar{v} and variance $\sigma_v^2 \ll \bar{v}^2$. The direction of motion was also defined as a random variable following a uniform distribution. The transitions between states were represented by two independent rates, namely k_{on} (switching rate between the non-motile to the motile state) and k_{off} (switching rate from motile to non-motile state). As a result the typical trajectories of those particles were a stochastic alternation of runs and pauses with a short time-scale ballistic motion and a long-time scale diffusive behavior. Unless stated otherwise, the set of parameters was: $k_{\text{on}} = 0.3 \text{ h}^{-1}$, $k_{\text{off}} = 0.2 \text{ h}^{-1}$, $\bar{v} = 10 \mu\text{m h}^{-1}$ and $\sigma_v = 5 \mu\text{m h}^{-1}$. The typical observation time was in the order of one hour, so that the dynamics was expected to be confined in the short time-scale regime.

2.6. Speckle computation

From cells dynamics simulations, the time-dependent speckle correlation was computed and compared with experimental data. Since the evolution time of the cellular structures is slow compared to the Thouless time (i.e. the light diffusion time through the system), each speckle was computed from the configuration of cells obtained at fixed time t . The autocorrelation of those speckles were then computed to calculate the time-dependent intensity correlation function. Since the cells dynamics involves large time scales compared to $2\pi/\omega$, with ω the frequency of the incident laser beam, there was a full decoupling between t (the time evolution of the structure) and ω .

To compute a speckle pattern, we first had to solve Maxwell's equations for an ensemble of cells. For that purpose, we chose to approximate each cell by a point scatterer in the electric-dipole limit. Strictly speaking, this approximation is valid under two conditions: the typical size of a cell is small compared to (1) the wavelength λ and (2) the average distance between two different cells. Since the samples used in the experiments did not meet these requirements, the computation of speckle patterns could not be used for precise quantifications. Nevertheless, this procedure is well-suited to retrieve general trends such as the decorrelation time as a function of the scattering vector. The optical response of a point dipole scatterer was described by its polarizability $\alpha(\omega)$, which links the dipole moment $\mathbf{p}(\omega, t)$ created inside the scatterer to the exciting electric field $\mathbf{E}^{(\text{exc})}(\omega, t)$ through the relation:

$$\mathbf{p}(\omega, t) = \epsilon_0 \alpha(\omega) \mathbf{E}^{(\text{exc})}(\omega, t), \quad (1)$$

where ϵ_0 is the vacuum permittivity. The polarizability was computed using the scattering cross-section given by

$$\sigma_s(\omega) = \frac{k_0^4}{6\pi} |\alpha(\omega)|^2, \quad (2)$$

where $k_0 = 2\pi/\lambda$ is the incident wavevector and λ the wavelength. $\alpha(\omega)$ is a complex number and a second equation is needed for its full determination. Due to energy conservation during the scattering process, the scattering cross-section must equal the extinction cross section (assuming a non-absorbing medium). This leads to

$$\sigma_e(\omega) = k_0 \text{Im} \alpha(\omega) = \sigma_s(\omega). \quad (3)$$

Using equations (2) and (3) we obtained the polarizability:

$$\alpha(\omega) = \frac{-6\pi}{k_0^3} \left[\sqrt{\frac{6\pi}{k_0^2 \sigma_s(\omega)} - 1} + i \right]^{-1}. \quad (4)$$

In principle, σ_s and σ_e can be determined from the geometry of the cell and its refractive index. Since this last quantity was not easily accessible experimentally, we chose to consider the scattering mean-free path instead, defined as

$$\ell_s(\omega) = \frac{1}{\rho \sigma_s(\omega)}, \quad (5)$$

where ρ is the density of scatterers. In the following, we consider a system composed of cells on a 2D surface, which is expected to fall into a single-scattering regime. For that reason, we chose to consider a large scattering mean-free path, i.e. $k_0 \ell_s = 1 \times 10^8$. We also assumed a density $\rho = (N/L^2)^{(3/2)}$ (2D density extrapolated in 3D), where $N \sim 100$ is the number of cells and $L = 868 \mu\text{m}$ the size of the system. Once the polarizability known, the coupled dipoles method was used to solve Maxwell's equations. It consisted in solving a linear set of coupled equations involving the exciting field $\mathbf{E}_j^{(\text{exc})}(\omega, t)$ on scatterer j lying at position \mathbf{r}_j . As reported in [24]:

$$\mathbf{E}_j^{(\text{exc})}(\omega, t) = \mathbf{E}_{\text{in}}(\mathbf{r}_j, \omega) + k_0^2 \alpha(\omega) \sum_{l=1, l \neq j}^N \mathbf{G}_0(\mathbf{r}_j(t) - \mathbf{r}_l(t), \omega) \mathbf{E}_l^{(\text{exc})}(\omega, t), \quad (6)$$

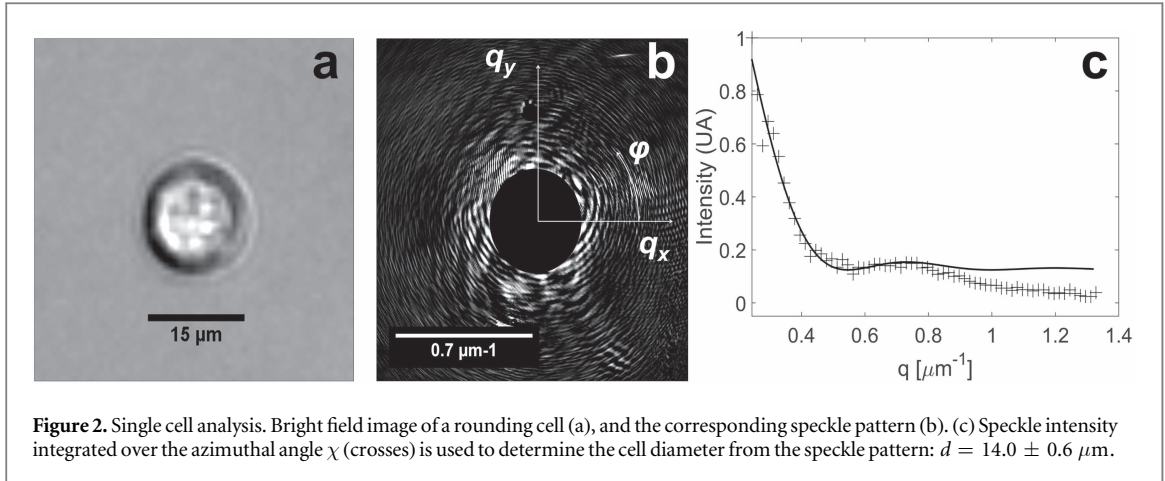
where \mathbf{G}_0 is the Green tensor in vacuum linking the electric field at any position in vacuum to a source dipole through the relation

$$\mathbf{E}(\mathbf{r}, \omega) = \mu_0 \omega^2 \mathbf{G}_0(\mathbf{r} - \mathbf{r}_0, \omega) \mathbf{p}_0(\omega), \quad (7)$$

where

$$\mathbf{G}_0(\mathbf{r} - \mathbf{r}_0, \omega) = \left[\mathbf{I} - \frac{\nabla_{\mathbf{r}} \otimes \nabla_{\mathbf{r}}}{k_0^2} \right] \frac{\exp[ik_0 |\mathbf{r} - \mathbf{r}_0|]}{4\pi |\mathbf{r} - \mathbf{r}_0|}, \quad (8)$$

\otimes denoting the tensor product operator. To be consistent with experimental conditions, the incident field $\mathbf{E}_{\text{in}}(\mathbf{r}, \omega)$ was chosen to be a gaussian beam of waist $w = 69 \mu\text{m}$ and wavevector \mathbf{k}_{in} . Once the exciting field on each scatterer was known, the field at any position inside or outside the system was computed using a relation similar to (6):



$$\mathbf{E}(\mathbf{r}, \omega, t) = \mathbf{E}_{\text{in}}(\mathbf{r}, \omega) + k_0^2 \alpha(\omega) \sum_{l=1}^N \mathbf{G}_0(\mathbf{r}(t) - \mathbf{r}_l(t), \omega) \mathbf{E}_l^{(\text{exc})}(\omega, t). \quad (9)$$

Considering an observation point \mathbf{r} in the far field (i.e. such that $r \gg \lambda$), the scattered field $\mathbf{E}_{\text{sca}} = \mathbf{E} - \mathbf{E}_{\text{in}}$ was simplified into

$$\mathbf{E}_{\text{sca}}(\mathbf{r}, \omega, t) = \frac{A}{k_0 r} \exp[ik_0 r] \mathbf{E}_{\text{sca}}(\mathbf{q}, \omega, t), \quad (10)$$

where A is a numerical constant, $\mathbf{q} = \mathbf{k}_{\text{out}} - \mathbf{k}_{\text{in}}$ is the scattering wavevector and $\mathbf{k}_{\text{out}} = k_0 \mathbf{r}/r$ the observation wavevector. Defining the scattered intensity by

$$I_{\text{sca}}(\mathbf{q}, \omega, t) = |\mathbf{E}_{\text{sca}}(\mathbf{q}, \omega, t)|^2 \quad (11)$$

we finally obtain the time-dependent intensity autocorrelation function

$$C(\mathbf{q}, \tau, \omega) = \frac{\langle I_{\text{sca}}(\mathbf{q}, \omega, t) I_{\text{sca}}(\mathbf{q}, \omega, t + \tau) \rangle}{\langle I_{\text{sca}}(\mathbf{q}, \omega, t) \rangle \langle I_{\text{sca}}(\mathbf{q}, \omega, t + \tau) \rangle} - 1, \quad (12)$$

where the brackets $\langle \dots \rangle$ denote the statistical average over all configurations of the cellular structure. This average was typically performed using 10 000 configurations generated using a run and tumble-like model. Assuming a statistical steady-state regime, C only depends on τ and not on t . It is important to note that, $I_{\text{sca}} = I$ and $\mathbf{E}_{\text{sca}} = \mathbf{E}$, with the exception of the forward direction. Thus in the following, I and \mathbf{E} are used to denote the scattered intensity and field respectively. For the sake of simplicity, the ω -dependence is also dropped.

3. Results

3.1. Speckle intensity

3.1.1. Isolated cell

We first observed the speckle pattern produced by a single rounding cell, which bright field image is shown in figure 2(a). The cell is illuminated with a vertical laser beam of wavevector \mathbf{k}_{in} , which modulus is $2\pi/\lambda$. The light scattered by the cell is collected in the forward direction by the CCD2 camera (figure 2(b)). Each pixel of the CCD2 camera corresponds to a different scattering angle and, thus, to a different wavevector \mathbf{k}_{out} . In this setup, the incident beam is superimposed on the low-angle scattering region of the speckle pattern. Due to saturation effects, this part was suppressed by applying a virtual beamstop at the center of the detector (black disk in the center of figure 2(b)). Background light is subtracted and vignetting effects are corrected [25]. We record the speckle pattern $I(\mathbf{q})$, $\mathbf{q} = \mathbf{k}_{\text{out}} - \mathbf{k}_{\text{in}}$ being the scattering wavevector.

As the rounding cell has spherical symmetry, we integrate the speckle pattern $I(\mathbf{q})$ over the azimuthal angle

$$I(q) = \int_0^{2\pi} I(q, \chi) d\chi, \quad (13)$$

where q is the magnitude of the vector \mathbf{q} and χ the azimuthal angle. The radial intensity profile $I(q)$ is plotted in figure 2(c) (crosses) and compared to the intensity profile expected for a scattering disk of diameter d :

$$\tilde{I}(q) \propto \left| J_1\left(\frac{qd}{2}\right) / \left(\frac{qd}{2}\right) \right|^2, \quad (14)$$

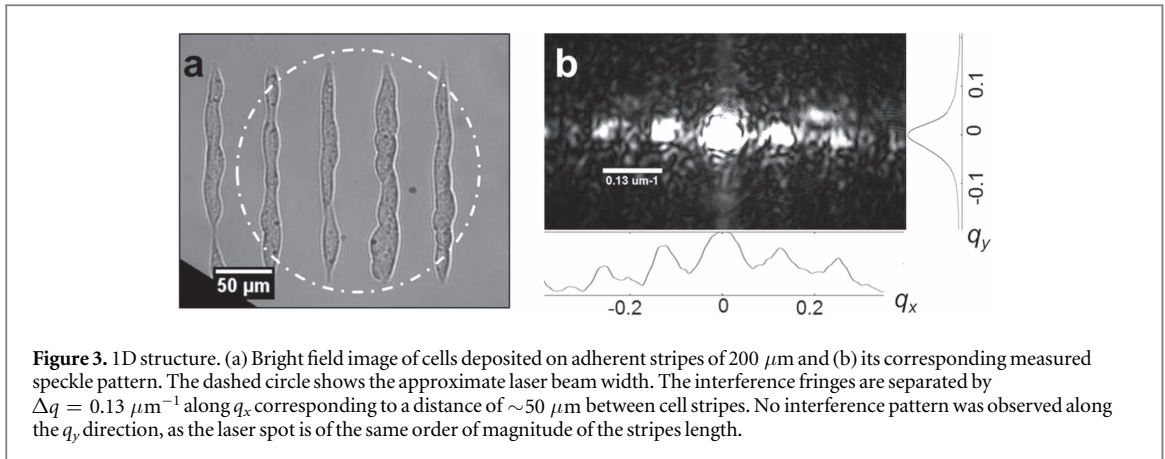


Figure 3. 1D structure. (a) Bright field image of cells deposited on adherent stripes of $200 \mu\text{m}$ and (b) its corresponding measured speckle pattern. The dashed circle shows the approximate laser beam width. The interference fringes are separated by $\Delta q = 0.13 \mu\text{m}^{-1}$ along q_x corresponding to a distance of $\sim 50 \mu\text{m}$ between cell stripes. No interference pattern was observed along the q_y direction, as the laser spot is of the same order of magnitude of the stripes length.

where J_1 is the Bessel function of order one. The best fit between the measured intensity $I(q)$ and the expected one $\tilde{I}(q)$ is obtained for a cell diameter $d = 14.0 \pm 0.6 \mu\text{m}$. This value is in good agreement with the cell diameter measured in figure 2(a), which is also $15 \pm 1 \mu\text{m}$.

At wavevectors larger than $1 \mu\text{m}^{-1}$, which correspond to distances smaller than $6.28 \mu\text{m}$ in direct space, the speckle pattern carries information, mostly related to the intracellular structure. As we aim at characterizing multicellular structures, collecting speckle patterns at $q < 1.2 \mu\text{m}^{-1}$ (set up limitation) is enough.

3.1.2. Cell on 1D lines

To create a simple and controlled multicellular structure, we deposited around 30 cells on adherent stripes prepared as stated in section 2. The stripes were $200 \mu\text{m}$ long, $10 \mu\text{m}$ wide and $50 \mu\text{m}$ apart from each other. The width was adjusted to accommodate at most one cell in the transversal direction and to produce a 1D cell lines. Figure 3(a) shows a bright field image of the aligned cells, and figure 3(b) the corresponding speckle pattern. The speckle pattern exhibits clear interference fringes along the q_x direction, separated by $\Delta q = 0.130 \pm 0.005 \mu\text{m}^{-1}$. This length corresponds to a distance of $48 \pm 2 \mu\text{m}$ in direct space, which matches the spacing between adherent stripes, within the experimental error. Interestingly, there are no interference fringes along the q_y direction. This is due to the fact that the laser spot has a width of $\sim 200 \mu\text{m}$ (see dashed circle in figure 3(a)) and therefore only illuminates a single row of stripes.

3.1.3. Sparse cells on a 2D surface

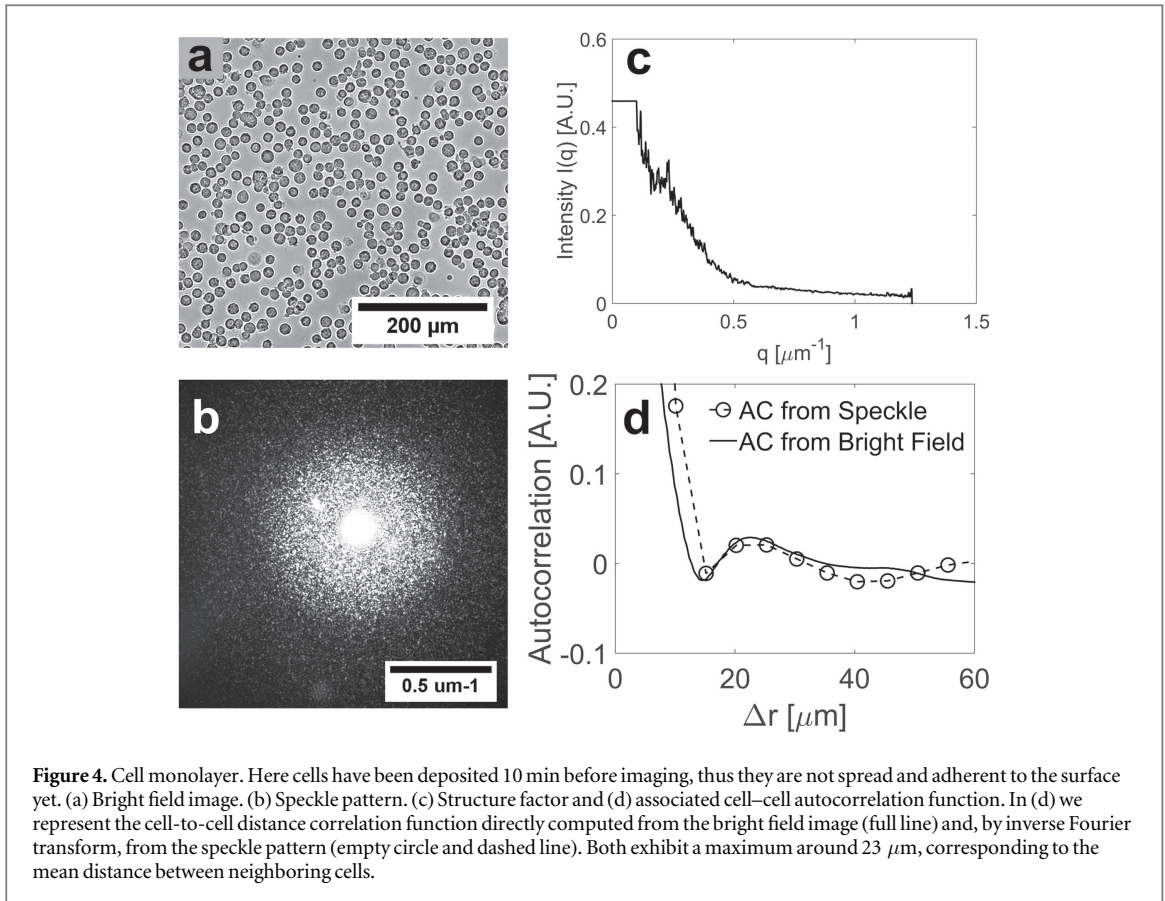
When cells are homogeneously deposited on a surface (figure 4(a)), the speckle pattern looks significantly different as compared to those in previous examples. The anisotropy induced by the stripes vanishes and, compared to that of a single cell, the speckle is characterized by an increased granularity. On the one hand, the typical grain size scales with the inverse of the laser beam width [26]. In this case, we chose to remove lenses to illuminate the sample with the full width of the laser (FWHM about $260 \mu\text{m}$) and thus probing a larger cell population. On the other hand, this granularity depends on the optical details of the illuminated area, but the overall decay is linked to the statistical properties of the multicellular structure. As we limit the acquisition to small wavevectors, filtering out the intracellular details, the cells appear as uniform scattering objects in first approximation. In the single scattering regime, the speckle intensity is related to the autocorrelation function of the surface cell density $P(\mathbf{r})$ through the equation

$$\langle P(\mathbf{r}')P(\mathbf{r} + \mathbf{r}') \rangle_{\mathbf{r}'} \propto \int I(\mathbf{q}) \exp[-i\mathbf{q} \cdot \mathbf{r}] d\mathbf{q}. \quad (15)$$

In figure 4(c) we report the azimuthally averaged speckle $I(q)$ together with the corresponding density–density autocorrelation function $P(\mathbf{r})$ (figure 4(d)). The incident beam ($q < 0.1 \mu\text{m}^{-1}$) is cut to not impair the autocorrelation function. When cells are sparse there is no spatial correlation between scatterers, but as the cell layer becomes confluent a typical cell-to-cell distance appears. Near the confluence point, the autocorrelation function exhibits a maximum corresponding to the mean distance between first neighbors. In the example shown in figure 4, this maximum happens at $r = 25 \pm 5 \mu\text{m}$ which is in good agreement with the correlation distances $r = 22.6 \mu\text{m}$ measured from the bright field image (continuous line).

3.2. Speckle fluctuation and cell motility

The cell movements inside the sample modifies the speckle pattern during the time sequence of acquisition. Thus, the details of the speckle dynamics depend on the trajectory of each cell. While the loss of phase information does not allow recovering single trajectories, the speckle intensity fluctuations are statistically



related to the kinetic properties of the multicellular ensembles. In this section, we derive an analytical expression to describe the time-dependent intensity correlation function under the assumptions that (1) the Siegert relation is valid and that (2) the system operates in the single-scattering regime. We also assume that the scalar approximation is valid and that the incident laser beam can be approximated by a plane-wave (valid in case of large waist).

For a fully developed speckle pattern, the electric field is statistically gaussian (which corresponds to a Rayleigh statistics for the intensity distribution) and the intensity–intensity correlation function factorizes into the square of the field–field correlation function $g_1(q, \tau)$, a result known as the Siegert relation. We have numerically checked that for all sets of parameters considered in this study (velocities, directions and times), the intensity statistics is exponential (Rayleigh distribution), only very slight deviations being observable. This proves the validity of the Siegert relation here. We end up with [27]

$$\begin{aligned}
 C(\mathbf{q}, \tau) &= \frac{\langle I(\mathbf{q}, t)I(\mathbf{q}, t + \tau) \rangle}{\langle I(\mathbf{q}, t) \rangle \langle I(\mathbf{q}, t + \tau) \rangle} - 1 \\
 &= \beta \left| \frac{\langle E(\mathbf{q}, t)E^*(\mathbf{q}, t + \tau) \rangle}{\langle E(\mathbf{q}, t)^2 \rangle} \right|^2 = \beta |g_1(\mathbf{q}, \tau)|^2,
 \end{aligned} \tag{16}$$

where β is the coherence factor of the experiment, which can be approximated to 1 as pixels are way smaller than speckles. In the single-scattering regime, the scattered electric field from an ensemble of N cells located at positions $\mathbf{r}_j(t)$ is a superposition of spherical waves with a resulting amplitude:

$$E(\mathbf{q}, t) \propto \sum_{j=1}^N e^{-i\mathbf{q}\cdot\mathbf{r}_j(t)}. \tag{17}$$

This can be easily obtained from (6), (9) and (10) removing the terms relative to multiple scattering. Thus, combining (16) and (17), we obtain

$$C(\mathbf{q}, \tau) = \left| \frac{S(\mathbf{q}, \tau)}{S(\mathbf{q}, 0)} \right|^2, \tag{18}$$

where

$$S(\mathbf{q}, \tau) \propto \left\langle \sum_{j,k} e^{-i\mathbf{q} \cdot [\mathbf{r}_j(t+\tau) - \mathbf{r}_k(t)]} \right\rangle. \quad (19)$$

It is worthwhile noting that the last term is proportional to the dynamical structure factor of the system. The displacement of j th cell over the elapsed time τ is defined as follows $\Delta \mathbf{r}_j(t + \tau) = \mathbf{r}_j(t + \tau) - \mathbf{r}_j(t)$. Thus assuming that all cells are identical and that the initial position $\mathbf{r}_j(t)$ of cells and their displacements $\Delta \mathbf{r}_j(t + \tau)$ are uncorrelated quantities, (19) turns into

$$S(\mathbf{q}, \tau) = S(\mathbf{q}, 0) \langle e^{-i\mathbf{q} \cdot \Delta \mathbf{r}(t+\tau)} \rangle \quad (20)$$

and (21) can be simplified to

$$C(\mathbf{q}, \tau) = |\langle e^{-i\mathbf{q} \cdot \Delta \mathbf{r}(t+\tau)} \rangle|^2. \quad (21)$$

The details of the dynamical behavior of cells is reflected in the intensity autocorrelation function. For instance particles moving in a persistent manner with an average speed \bar{v} have net displacement $\Delta \mathbf{r}(\tau) = \mathbf{v}\tau$. Thereby the characteristic correlation time $\tau_{1/2}$, chosen to be the width at half maximum of the correlation function, scales as $\tau_{1/2} \propto 1/\bar{v}q$ (see figure 5(b), (d)). In the case of immobile particles, the displacements $\Delta \mathbf{r}(\tau)$ are null rendering to a correlation time scale $\tau_{1/2}$ independent of the wavenumber q (see figure 5(d)). Alternatively, in the case of an ensemble of Brownian particles with a diffusion coefficient D , the mean squared displacement is $\langle \Delta r^2(\tau) \rangle = 2D\tau$. Thus the characteristic correlation time $\tau_{1/2}$ scales as $\tau_{1/2} \propto 1/Dq^2$. Hence, in three cases a power law relationship relates the correlation time to the scattering wavevector $\tau_{1/2} \propto q^{-n}$ with n equals to 0, 1 or 2 accordingly. These three scenarios may coexist in the same multicellular ensemble at different time or length scales. In the following we propose two examples to illustrate this approach.

3.2.1. Cells deposited on the surface

We monitor the speckle pattern of a layer of cells uniformly spread on a surface (see figure 4(a)). Four petri dishes were seeded at different concentrations (2 ml with 150×10^3 , 300×10^3 , 600×10^3 and 10^6 cells respectively) and incubated for 24 h. After incubation, we measure the confluence degree as the percentage of the surface covered by cells.

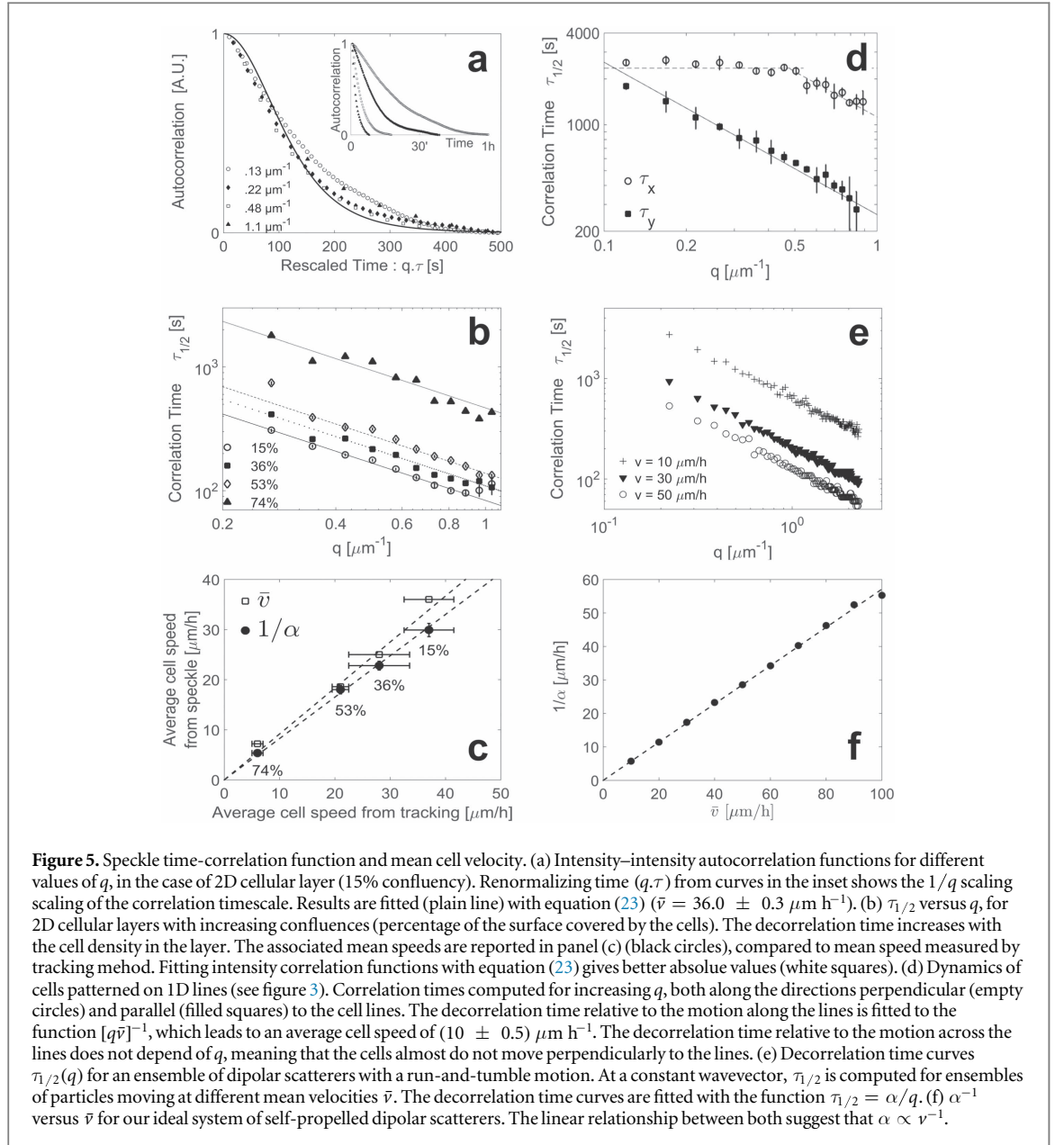
As we are only interested in the decorrelation time, we normalize $C(\mathbf{q}, \tau)$ to 1 at the origin. The less confluent samples are reported in the inset of figure 5(a) for four different values of the scattering wavevector q . The set of measured correlation functions collapse into a single master curve after scaling the time τ by the factor q^{-1} (see figure 5(a)), which means that the characteristic correlation time scales as $\tau_{1/2} \propto 1/q$, thus cells moves in a persistent manner. This may come as a surprise as we do not see this ballistic motion when watching cells moving, but rather a run and tumble motion. The reason is that intensity decorrelates within times (from 100 to 300 s) shorter than the average running time (1000 s). In this short time regime, displacements are dominated by ballistic runs. The power law is also apparent in figure 5(b), where the q -dependance of $\tau_{1/2}$ are reported for the different degrees of confluence. For values of q within the range $0.1 \mu\text{m}^{-1} < q < 1.1 \mu\text{m}^{-1}$, we find a power law with an exponent close to -1 , for any degree of confluency (lines). This means that cells move ballistically over these timescales, regardless of the local cell density.

By fitting the curve $\tau_{1/2} = \alpha/q$, we estimate the mean velocity of cells as $\bar{v} = 1/\alpha$, as explained in the previous section. Compared to the average cell speed obtained from single cell tracking, relative values are accurate ($< 5\%$). However absolute values are systematically underestimated by 18% (figure 5(c)) because the exact pre-factor is unknown. Figure 5(b) shows that \bar{v} depends on the cell density so that the denser the layer, the smaller the average cell's speed. This effect may either indicate that the internal friction of the cell layer increases with density, or that collisions between cells occur more often, slowing them down.

In order to obtain the exact pre-factor, we build from equation (21) using the ballistic regime property $\Delta \mathbf{r}(\tau) = \mathbf{v}\tau$. Notice that those displacements are independent of the initial time t and only depend on the elapsed time τ . In the absence of external cues, all directions are equally probable and thus the initial orientation of cells turns into a uniformly distributed random variable. For empirical reasons, the cell speed v will be also treated as an independent random variable obeying an exponential distribution $f(v) = \frac{4}{v^2} e^{-2v/\bar{v}}$ with a mean speed \bar{v} . Under these assumptions, the average over all the possible configurations in (21) can be replaced by the average over these internal variables

$$\langle e^{-i\mathbf{q} \cdot \Delta \mathbf{r}(\tau)} \rangle = \frac{1}{2\pi} \int_0^{2\pi} \int_0^\infty e^{-i\mathbf{q}v\tau \cos \zeta} f(v) v dv d\zeta, \quad (22)$$

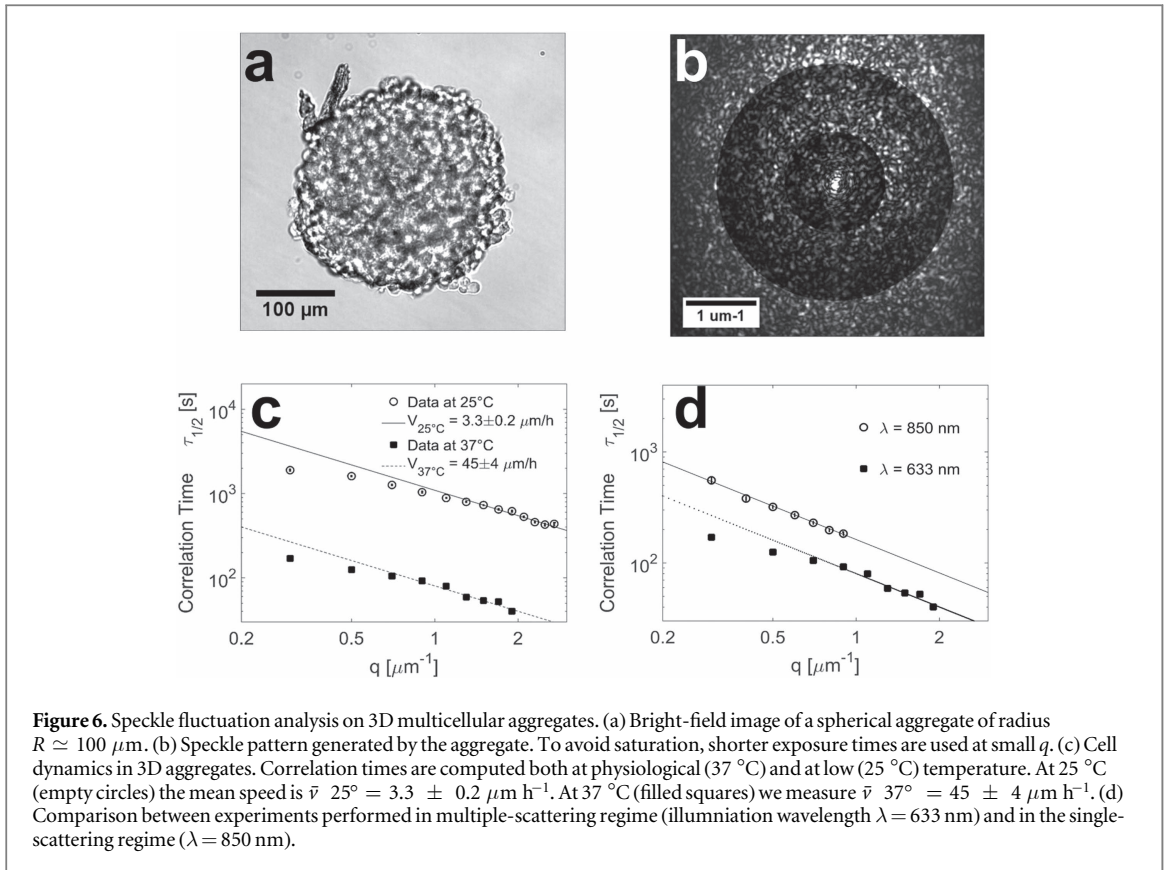
ζ being the angle between the direction of motion and \mathbf{q} the scattered wavevector. The intensity autocorrelation function of our ensemble of particles can be computed analytically and it reads



$$C(\mathbf{q}, \tau) = |\langle e^{-i\mathbf{q}\cdot\Delta\mathbf{r}(\tau)} \rangle|^2 = \left[1 + \left(\frac{q\bar{v}\tau}{2} \right)^2 \right]^{-3}, \quad (23)$$

which is univocally related to a single characteristic time scale of the system $\tau_{1/2} \simeq 1/q\bar{v}$, as expected for ballistic motion. Fitting intensity correlation functions in figure 5(a) using (23), we find $\bar{v} = 36.0 \pm 0.3 \mu\text{m h}^{-1}$. The master curve is in excellent agreement with the analytical expression, meaning that the behavior of our ensemble of cells is compatible with a system of dipole scatterers moving at constant speed with the speed distribution $f(v)$. Using equation (23), the pre-factor is almost corrected (underestimated by 8%) (figure 5(c)). Notice that if a relative measurement or an approximate absolute value is enough, fitting directly $\tau_{1/2}(q)$ has the advantage of being free of any modeling efforts or peculiar hypotheses on the ballistic movement.

Those observations are in agreement with the behavior of an ideal system of point dipole scatterers with a run-and-tumble-like dynamics. Accordingly, we computed the time-dependent autocorrelation functions $C(\mathbf{q}, \tau)$ and its width at half maximum $\tau_{1/2}$ with a coupled-dipoles method. They are reported as a function of the wavevector q in figure 5(e). For all analyzed cases, the behavior of $\tau_{1/2}$ follows this of $1/q$ for more than one decade, meaning that our particles move in a ballistic manner over shorter timescales than the tumbling time. Thus, $\tau_{1/2} = \alpha/q$ where α is thought to be inversely proportional to the mean particle's speed \bar{v} . In order to validate the generality of this relationship, we computed the coefficient α of the curves $\tau_{1/2}(q)$ for different values of \bar{v} . The results displayed in figure 5(f) show the linear dependence between $1/\alpha$ and \bar{v} for velocities between 10 and 100 $\mu\text{m h}^{-1}$. The slope deviates from 1 as it is a quantity dependent on this specific model.



3.2.2. Cells on stripes

Another interesting example is provided by the experiment illustrated in figure 3. The cells are deposited on adherent lines, which induce a strong anisotropic structural arrangement. The anisotropy found in the speckle pattern (figure 3(b)), is also visible in the dynamic structure factor or, experimentally, in the intensity-intensity autocorrelation function. Plotting $C(q, \tau)$ as a function of q , we observe two different behaviors along the directions parallel (q_{\parallel}) or perpendicular (q_{\perp}) to the stripes. Along q_{\parallel} (vertical direction in figure 3), the decorrelation time decreases proportionally to q_{\parallel}^{-1} (filled squares in figure 5(d)), meaning that cells move directionally along the lines. The theoretical best agreement between the experimental data and the power law $\tau_{1/2} = [q\bar{v}]^{-1}$ is obtained for a mean speed $\bar{v} = (10 \pm 0.5) \mu\text{m h}^{-1}$. On the contrary, along the direction perpendicular to the stripes the correlation time is independent of the scattering wavevector q_{\perp} (see figure 5(d), empty circles). This indicates that the cells do not move along this direction (horizontal in figure 3) due to the confinement imposed by the adherent stripes. Nevertheless, there is a noticeable decrease of the correlation time at q_{\perp} larger than $0.55 \mu\text{m}^{-1}$. In the real space this corresponds to 11.5μ , which is very close to the stripes width ($10 \mu\text{m}$). This is compatible with a residual motility of the cells along the perpendicular direction, provided that they do not exit the adherent stripes.

3.2.3. 3D aggregates

Analysis of speckle fluctuation is specially relevant in three-dimensional multicellular structures, where video microscopy cannot easily measure cell speed. As a proof of concept, we apply the method to multicellular spheroids (figure 6(a)), equation (21) being also valid in three dimensions. The speckle pattern produced by the spheroid is shown in figure 6(b). The scattered intensity drops considerably at large q . To preserve the signal-to-noise ratio at large q and to avoid saturation at low q , the exposure time changes with the scattering angle, (see rings of different intensities in figure 6(b)). In order to modulate cell activity and speed, the experiment is performed at two different temperatures: the physiological 37°C and 25°C , where cell activity almost vanishes. Figure 6(c) displays the decorrelation time $\tau_{1/2}(q)$, both for experiments done at 25°C (empty circles, error bars inside the circles) and at 37°C (black squares). In both cases, the experimental data scales reasonably well with the inverse of the scattering vector. From figure 6(c) we deduce that the mean speed \bar{v} increases considerably with the temperature. In particular, at 25°C the best fit between the theoretical curve and the data is obtained for a speed $\bar{v}^{25^\circ} = 3.3 \pm 0.2 \mu\text{m h}^{-1}$ (continuous line), while at 37°C we measure $\bar{v}^{37^\circ} = 45 \pm 4 \mu\text{m h}^{-1}$ (dashed line). Due to the presence of multiple-scattering events, this speed is overestimated. As described by Pine et al [28], the decorrelation time varies inversely to the number of scattering events. With a wavelength

$\lambda = 633$ nm, the mean free-path of photons $\ell_p \simeq 60 \mu\text{m}$ is four times smaller than the spheroid diameter. Thus, the measurement is semi-quantitative and allows one to compare velocities in the same sample, but under different conditions (e.g. temperature, mechanical stress, confinement, drugs, ...). Multiple scattering also impacts the q -dependency of $\tau_{1/2}$ at low q , where a deviation from the theoretical curve appears ($q < 0.5 \mu\text{m}^{-1}$ in figure 6(c)). For an absolute measurement of the cell speed and to avoid the deviation at low q , the illumination wavelength λ must be tuned to satisfy the single-scattering condition, i.e. a mean free-path of photons comparable to the spheroid size ($\ell_p \geq D$). In CT26 spheroids with a diameter of $\sim 250 \mu\text{m}$, this condition is satisfied for $\lambda = 850$ nm, at which $\ell_p \simeq 220 \mu\text{m}$. As show in figure 6(d), at this wavelength the deviation at low q vanishes and we measure a mean cell velocity of $\sim 20 \mu\text{m h}^{-1}$, comparable to that of single adherent cells.

4. Conclusion

The examples presented here show that cellular structures produce a clear and exploitable diffraction signal. This approach represents a valuable alternative to optical microscopy to measure the structure and the dynamics at the supracellular scale. Speckle analysis does not require image analysis and segmentation and it is self-averaging. This makes it a fast technique suitable to compare large sets of samples prepared under different conditions (drugs, temperature, genetic mutations or mechanical perturbations). It is also promising for investigating the dynamics of 3D multicellular samples, where microscopy is limited in term of sample thickness, staining and light dose. In the most basic version, the experimental setup is also compact (a laser diode and a CMOS detector) and fits in a standard incubator.

Acknowledgments

We thank François Ingremeau, Arnaud Millet, Monika Dolega, Jacques Derouard and Erik Geissler for helpful discussions. The research was supported by LABEX WIFI (Laboratory of Excellence within the French Program ‘Investments for the Future’) under references ANR-10-LABX-24 and ANR-10-IDEX-0001-02 PSL*, by the Agence Nationale pour la Recherche (Grant ANR-13-BSV5-0008-447 01), the Institut National de la Santé et de la Recherche Médicale (Grant 2011-1-PL BIO-448 11-IC-1) and by the Centre National de la Recherche Scientifique (‘Programme Emergence 2016’).

ORCID

Aurélien Gourrier  <https://orcid.org/0000-0001-9526-5746>

References

- [1] Friedl P, Sahai E, Weiss S and Yamada K M 2012 New dimensions in cell migration *Nat. Rev. Mol. Cell Biol.* **13** 743–7
- [2] Delarue M, Montel F, Caen O, Elgeti J, Siaugue J-M, Vignjevic D, Prost J, Joanny J-F and Cappello G 2013 Mechanical control of cell flow in multicellular spheroids *Phys. Rev. Lett.* **110** 138103
- [3] Meijering E et al 2012 Methods for cell and particle tracking *Methods Enzymol.* **504** 183–200
- [4] Fournet G and Guinier A 1955 *Small Angle Scattering of X-Rays* (New York: Wiley) pp 7–78 Translated by Walker C B and Yudowitch K L
- [5] Glatter O and Kratky O 1982 *Small Angle X-Ray Scattering* (London: Academic)
- [6] Feigin L A, Svergun D I and Taylor G W 1987 *Structure Analysis by Small-Angle X-Ray and Neutron Scattering* (Berlin: Springer)
- [7] Steinkamp J A 1984 Flow cytometry *Rev. Sci. Instrum.* **55** 1375–400
- [8] Xu M, Wu T T and Qu J Y 2008 Unified mie and fractal scattering by cells and experimental study on application in optical characterization of cellular and subcellular structures *J. Biomed. Opt.* **13** 024015
- [9] Perelman L T 2006 Optical diagnostic technology based on light scattering spectroscopy for early cancer detection *Expert Rev. Med. Devices* **3** 787–803
- [10] Wax A and Backman V 2015 *Biomedical Applications of Light Scattering IX* vol 9333 (Bellingham WA: SPIE Press) <http://spie.org/Publications/Proceedings/Volume/9333>
- [11] Berne B J and Pecora R 1976 *Dynamic Light Scattering: With Applications to Chemistry, Biology, and Physics* (Mineola, NY: Dover)
- [12] Conrad H, Lehmkuhler F, Fischer B, Westermeier F, Schroer M A, Chushkin Y, Gutt C, Sprung M and Grubel G 2015 Correlated heterogeneous dynamics in glass-forming polymers *Phys. Rev. E* **91** 042309
- [13] Tamborini E and Cipelletti L 2012 Multiangle static and dynamic light scattering in the intermediate scattering angle range *Rev. Sci. Instrum.* **83** 093106
- [14] Li J, Dietsche G, Iftime D, Skipetrov S E, Maret G, Elbert T, Rockstroh B and Gisler T 2005 Noninvasive detection of functional brain activity with near-infrared diffusing-wave spectroscopy *J. Biomed. Opt.* **20** 044002
- [15] Weber B, Burger C, Wyss M T, von Schulthess G K, Scheffold F and Buck A 2004 Optical imaging of the spatiotemporal dynamics of cerebral blood flow and oxidative metabolism in the rat barrel cortex *Eur. J. Neurosci.* **20** 2664

- [16] Jaillon F, Skipetrov S E, Li J, Dietsche G, Maret G and Gisler T 2001 Diffusing-wave spectroscopy from head-like tissue phantoms: influence of a non-scattering layer *Opt. Express* **14** 10181
- [17] Suissa M, Place C, Goillot E and Freysingheas E 2008 Internal dynamics of a living cell nucleus investigated by dynamic light scattering *Eur. Phys. J. E* **26** 435–48
- [18] Nolte D D, An R, Turek J and Jeong K 2011 Holographic tissue dynamics spectroscopy *J. Biomed. Opt.* **16** 087004
- [19] Lee J, Radhakrishnan H, Wu W, Daneshmand A, Klimov M, Ayata C and Boas D A 2013 Quantitative imaging of cerebral blood flow velocity and intracellular motility using dynamic light scattering–optical coherence tomography *J. Cereb. Blood Flow Metab.* **33** 819–25
- [20] Martinez V A, Besseling R, Croze O A, Tailleux J, Reufer M, Schwarz-Linek J, Wilson L G, Bees M A and Poon W C K 2012 Differential dynamic microscopy: a high-throughput method for characterizing the motility of microorganisms *Biophys. J.* **103** 1637–47
- [21] Mourant J R, Johnson T M, Doddi V and Freyer J P 2002 Angular dependent light scattering from multicellular spheroids *J. Biomed. Opt.* **7** 93–9
- [22] Tseng Q, Wang I, Duchemin-Pelletier E, Azioune A, Carpi N, Gao J, Filhol O, Piel M, Théry M and Balland M 2011 A new micropatterning method of soft substrates reveals that different tumorigenic signals can promote or reduce cell contraction levels *Lab Chip* **11** 2231–40
- [23] Cipelletti L and Weitz D A 1999 Ultralow-angle dynamic light scattering with a charge coupled device camera based multispeckle, multitaup correlator *Rev. Sci. Instrum.* **70** 3214–21
- [24] Lax M 1952 Multiple scattering of waves: II. The effective field in dense systems *Phys. Rev.* **85** 621
- [25] Ferri F 1997 Use of a charge coupled device camera for low-angle elastic light scattering *Rev. Sci. Instrum.* **68** 2265–74
- [26] Goodman J W 1976 Some fundamental properties of speckle *J. Opt. Soc. Am.* **66** 1145–50
- [27] Ventsel H 1973 *Théorie des probabilités* (Moscou: Mir)
- [28] Pine D J, Weitz D A, Zhu J X and Herbolzheimer E 1990 Diffusing-wave spectroscopy: dynamic light scattering in the multiple scattering limit *J. Phys.* **51** 2101–27